

Check for updates

2-Bromonaphthalene-Induced Defect Passivation to Suppress Ion Migration in CsPbBr₃ Wafer for X-Ray Detector with Bias-Resistant Stability

Xiao Zhao, Ziqing Li, Shimao Wang,* Yanan Song, Enliu Hong, Tingting Yan, Gang Meng,* and Xiaosheng Fang*

Featuring exceptional photoelectronic properties and scalability, hot-pressing processed all-inorganic (i. e., CsPbBr₃) perovskite wafers have emerged as promising candidates for direct X-ray imaging. Nonetheless, severe ion migration in CsPbBr₃ wafers results in a large and drifting dark current, thereby compromising the bias-resistant stability of the X-ray detector. Herein, a solvent-free interfacial defect passivation strategy is proposed by introducing a passivator molecule, 2-bromonaphthalene, to passivate interfacial defects and suppress ion migration in CsPbBr₃ wafers. Implementing this strategy effectively inhibits ion migration in CsPbBr₃ wafers, as evidenced by an enhanced ion migration activation energy of 0.56 eV and a negligible dark-current drift of 4.01 \times 10⁻⁸ μ A cm⁻¹ s⁻¹ V⁻¹, representing a 100 fold reduction in dark current drift compared to untreated CsPbBr₃ wafers under a high electric field of 100 V mm⁻¹; indicating a high bias-resistant stability. Consequently, the CsPbBr₃ wafer X-ray detector achieves an impressively high sensitivity of 11090 μC Gy_{air}⁻¹ cm⁻², a low detection limit of 9.41 nGy_{air} s⁻¹ under a 100 V mm⁻¹ electric field, and high-contrast X-ray imaging capabilities, with performance comparable to that of CsPbBr₃ single-crystal-based X-ray detector, highlighting the potential of interfacial defect passivation strategy for high-performance X-ray detectors.

1. Introduction

X-ray detection has been extensively applied in medical diagnostics, security inspections, nondestructive examination of

X. Zhao, S. Wang, Y. Song, G. Meng Anhui Provincial Key Laboratory of Photonic Devices and Materials Anhui Institute of Optics and Fine Mechanics

and Key Laboratory of Photovoltaic and Energy Conservation Materials Hefei Institutes of Physical Science

Chinese Academy of Sciences Hefei 230031, P. R. China

E-mail: shmwang@aiofm.ac.cn; menggang@aiofm.ac.cn

X. Zhao, Z. Li, E. Hong, T. Yan, X. Fang Department of Materials Science State Key Laboratory of Molecular Engineering of Polymers and Institute of Optoelectronics Fudan University

Shanghai 200433, P. R. China E-mail: xshfang@fudan.edu.cn

The ORCID identification number(s) for the author(s) of this article can be found under https://doi.org/10.1002/adfm.202500039

DOI: 10.1002/adfm.202500039

industrial production, and scientific research.[1-3] To reduce the potential risks associated with X-ray exposure, it is essential to develop X-ray detectors with a high signal-to-noise ratio (SNR), high sensitivity, and an ultralow detection limit to minimize the required X-ray dosage. Recently, metal halide perovskite single crystals (SCs) have garnered significant attention as promising materials for high-performance direct X-ray detection by virtue of high X-ray attenuation capability,[4,5] large carrier mobility-lifetime products $(\mu\tau)$, [6,7] low-temperature solution processability,[8] and cost-effectiveness.[9] Despite these advances, the size scalability of perovskite SCs remains a critical bottleneck for large-area device applications, primarily due to the time-consuming and complicated crystal growth processes required.[10]

Considering the X-ray refractive index being \approx 1.0 and the associated challenges in focusing, it is imperative for X-ray flat-panel detectors to achieve scalability in alignment

with the dimensions of the objects being examined, especially in commercial applications, such as medical diagnostics and industrial inspections.[11-13] Solution-processed perovskite polycrystalline thick films with scalable areas can be readily fabricated using various techniques, including blade coating,[14] spray-coating,[15] screen printing,[16] and roll-to-roll processing. [17] However, solution-processing methods encounter significant challenges in fabricating high-quality, uniform films with millimeter-scale thickness. A major difficulty is the solvent evaporation during film preparation, which inevitably leads to the formation of pinholes and cracks. [18] These defects substantially impede charge carrier transport and degrade the photoelectronic properties of the thick films. Previous studies have shown that CsPbBr₃ films produced by the mist deposition method also meet the requirements of large-area, thick-film, and low-cost fabrication while enabling oriented film formation.[19] From a practical application perspective, solvent-free powder-pressed perovskite polycrystalline wafers present a more facile, cost-effective, timeefficient, and scalable alternative to SCs, while being more uniform and compact compared to solution-processed perovskite polycrystalline thick films.^[20] By tuning the dimensions and geometry of the mold, as well as optimizing the powder loading,

16163028, 2025, 33. Downladed from https://advanced.onlinelibrary.wiley.com/doi/10.1002/afm.202500039 by Fudat University, Wiley Online Library on [28.09/2025], See the Terms and Conditions (https://onlinelibrary.wiley.com/terms-and-conditions) on Wiley Online Library for rules of use; OA articles are governed by the applicable Creative Commons Licensity (Commons Licensity Commons Licens

dense and phase-pure perovskite wafers with customizable sizes, shapes, and thicknesses can be fabricated. [21,22]

Nevertheless, due to its ionic nature and relatively low activation energy, ion migration is an inevitable issue in perovskite wafers.^[23] Even worse, grain boundaries in perovskite wafers can provide pathways for mobile ionic defects, which leads to increased ionic conductivity, elevated dark current, higher noise, and substantial current baseline drift, all of which deteriorate device performance and compromise long-term operational stability. It has been reported that lowering the electronic dimensionality of halide perovskite structures can effectively mitigate or suppress ion migration.^[24] Low-dimensional halide perovskite materials, such as 0D MA₃Bi₂I₀, [24,25] Cs₃Bi₂I₀, [26] 2D $(C_6H_5C_2H_4NH_3)_2PbX_4$ $((PEA)_2PbX_4, X=Cl, Br, I),^{[27,28]}$ and (NH₄)₃Bi₂I₉, [29] have demonstrated suppressed ion migration and stable dark current baseline, resulting in impressively low detection limits below 100 nGy_{air} s⁻¹.[30] Despite these advancements, the intrinsic anisotropy and inferior carrier transport properties of low-dimensional perovskite lead to significantly lower X-ray sensitivities compared to their 3D counterparts.[30,31] Among the various 3D halide perovskites, all-inorganic perovskite CsPbBr3 has emerged as a highly competitive material for X/γ -ray detection, owing to its superior photoelectric properties, excellent humidity resistance, high thermal stability, and significantly enhanced chemical stability compared to organicinorganic halide perovskites.^[5,32] However, the presence of grain boundaries and abundant defects can induce severe ion migration under biased operational conditions, resulting in large and fluctuating dark currents, which deteriorate both the detection limits and the long-term operational stability of devices.[33] Moreover, the enhancement of charge collection efficiency in semiconductor X-ray detectors often necessitates the application of high electric fields, which, however, exacerbate ion migration and compromise device stability. Several strategies, including mixed halogen, [34] CsPbBr₃-based heterostructures, [35–37] and atmosphere-controlled growth techniques [38,39] have been explored to mitigate ion migration or passivate defects. Despite these advances, addressing interfacial defects (the primary pathways for ion migration) in area-scalable CsPbBr3 wafers remains a significant challenge. Tackling this issue is crucial for overcoming the limitations posed by ion migration and is essential for achieving high-performance CsPbBr₃ wafer-based X-ray detectors with enhanced photoelectronic properties and long-term operational stability.

In this work, a solvent-free interfacial defect passivation strategy is proposed to tackle the critical challenges of interfacial defects and ion migration in CsPbBr₃ wafers by incorporating 2- bromonaphthalene. This additive, characterized by its nonvolatile nature and low melting point, facilitates electron transfer from its electron-rich bromine atoms to defective Pb²⁺ sites, thereby reducing defect densities. The impact of 2-bromonaphthalene introduction on passivating interfacial defects and suppressing ion migration is comprehensively investigated. Subsequently, X-ray detectors based on the treated CsPbBr₃ wafers are fabricated, and their X-ray detection performance and imaging capabilities devices are systematically evaluated.

2. Results and Discussion

The preparation process for the CsPbBr₃ polycrystalline wafer is schematically illustrated in Figure 1a. Initially, bar-shaped CsPbBr₃ SCs, grown via the anti-solvent diffusion-assisted crystallization method (Figure S1, Supporting Information),^[21] are ground together with 2-bromonaphthalene powders to form a homogenous mixture. This mixture is then loaded into a steel mold and subjected to compression at 10 MPa and 80 °C for 1 h. Owing to its low melting point, 2-bromonaphthalene infiltrates vertically throughout the wafer during the hot-pressed process, effectively filling the grain boundaries of the CsPbBr, wafer. As expected, the combined effects of heat and pressure result in the formation of dense and uniform CsPbBr3 wafers, as shown in Figure 1b. The resulting CsPbBr3 wafers are circular with a diameter of 1 cm, and their thickness can be adjusted by varying the amount of powder loaded. Additionally, using CsPbBr₂ SCs as the raw material for hot pressing helps reduce defects within the grains and enhances the crystallization quality of the wafers. As shown in Figure \$3 (Supporting Information), the diffraction peaks of the obtained CsPbBr₃ wafer match the standard diffraction patterns of CsPbBr₂ with an orthorhombic structure (ICSD, #97851). Notably, additional diffraction peaks at 11.60° are observed in the XRD patterns for CsPbBr3 wafers with varying molar ratios of 2-bromonaphthalene, which are attributed to the incorporation of this additive. These results indicate that the infiltration of 2-bromonaphthalene molecules into neighboring intergrain regions during the 1 h hot-pressed process does not alter the crystal phase, cause decomposition of CsPbBr₃, or generate new crystalline phases.

Nevertheless, excessive passivation agents typically result in reduced conductivity and impaired charge transport within devices.[41] To determine the optimal amount, Au/CsPbBr₂ wafer/Au symmetric electrode devices have been fabricated, as illustrated in Figures S4, S5 (Supporting Information), to evaluate their electrical properties. In general, high resistivity is advantageous for reducing dark current and suppressing noise current, thereby improving the SNR, while a high $\mu\tau$ product facilitates efficient charge carrier collection. The resistivity and $\mu\tau$ products of CsPbBr₃ wafers with varying 2-bromonaphthalene molar ratios have been fitted (Figures S6, S7, Supporting Information). The detailed results have been summarized in Table 1. Upon analysis, a 2-bromonaphthalene molar ratio of 3% is identified as optimal, yielding excellent charge carrier transport with a $\mu \tau$ product of 3.97×10^{-3} cm² V⁻¹ and a high resistivity of 4.89×10^{9} Ω cm, closely approaching those of CsPbBr, SCs. $^{[\dot{3}\dot{3},38,42]}$ Accordingly, the subsequent discussion presents a comparative analysis between the control CsPbBr3 wafer, which was prepared without the addition of 2-bromonaphthalene, and the target CsPbBr₃ wafer containing a 3% molar ratio of 2-bromonaphthalene.

Grain boundaries in polycrystalline wafers can significantly degrade electronic properties, including carrier mobility, lifetime, and collection efficiency, due to interfacial defects that act as carrier traps.^[11,43] These defects introduce localized energy states, leading to potential fluctuations that elevate the interfacial transport barrier, increase recombination rates, and reduce carrier drift, ultimately impairing device performance.^[44,45] To

16163028, 2025, 33, Downloaded from https://advanced.onlinelibrary.wiley.com/doi/10.1002/adfm.202590039 by Fudan University, Wiley Online Library on [28.09/2025]. See the Terms and Conditions (https://onlinelibrary.wiley

und-conditions) on Wiley Online Library for rules of use; OA articles are governed by the applicable Creative Commons

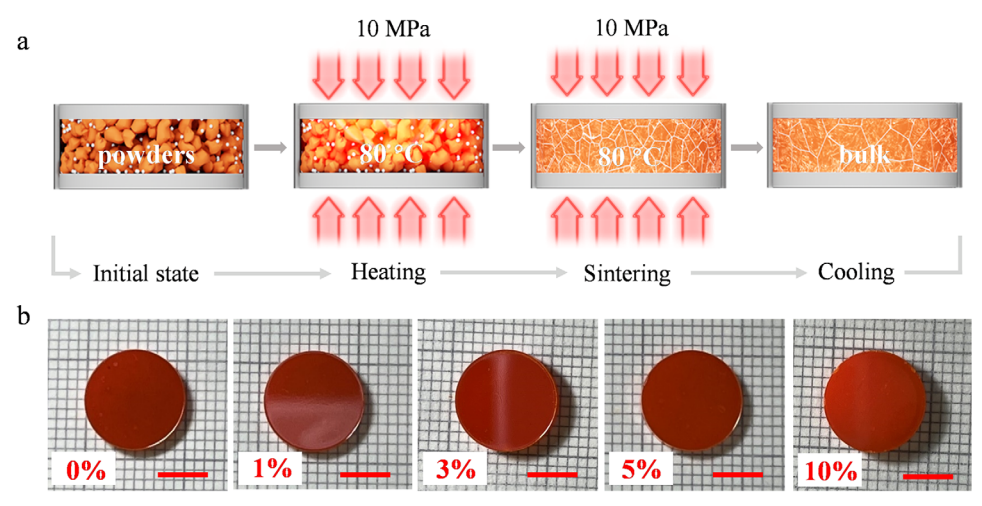


Figure 1. a) Schematic of the preparation process for CsPbBr₃ wafers. b) Photographs of CsPbBr₃ wafers with different molar ratios of 2-bromonaphthalene. The scale bar is 5 mm.

evaluate the effect of 2-bromonaphthalene incorporation on the microstructural morphology of CsPbBr3 wafers, cross-sectional scanning electron microscopy (SEM) measurements have been performed on both control and target CsPbBr3 wafers. The SEM images of the control CsPbBr3 wafer reveal a compact structure with distinct grain boundaries and minimal porosity between the grains (Figure 2a,b). In contrast, as depicted in Figure 2c,d, the introduction of 2-bromonaphthalene results in increased grain size, less distinct grain boundaries, and the dispersion of 2bromonaphthalene along the grain edges. The observed grain enlargement following 2-bromonaphthalene incorporation can be attributed to modified grain growth kinetics, including reduced grain boundary migration resistance and the potential influence of 2-bromonaphthalene in stress release, thereby creating a more stable environment for grain expansion.^[46] The increased grain size in the target CsPbBr₃ wafer is beneficial for enhancing carrier transport and charge collection efficiency, ultimately improving the overall electronic performance of the devices.

To evaluate the impact of interfacial defect passivation on charge recombination in control and target CsPbBr₃ wafers, steady-state photoluminescence (PL) spectroscopy measurements have been performed. As shown in Figure 2e, the target wafer exhibits higher PL intensity and a blueshifted PL peak compared to the control. The increased PL intensity indicates reduced nonradiative recombination due to the passivation of defect states like surface traps and grain boundary defects. Fewer defects limit nonradiative pathways, thereby enhancing radiative recombination. Additionally, the blueshift suggests that defect passivation diminishes band tailing from localized states within the bandgap.

This reduction in defect-related states ensures that PL emission is dominated by band-to-band transitions closer to the intrinsic bandgap of CsPbBr₃, resulting in higher emission energies. [47,48] Additionally, time-resolved photoluminescence (TRPL) measurements have been conducted (Figure 2f). The target CsPbBr₃ wafer demonstrates an extended carrier radiative recombination lifetime of 50.43 ns, significantly longer than that of the control CsPbBr₃ wafer (23.13 ns), indicating better charge carrier dynamic properties, further confirming the effective passivation capability of 2-bromonaphthalene. Figure 2g presents the trap density ($N_{\rm trap}$) determined by the space-charges-limited-current (SCLC) method. The trap-filled limit voltage ($V_{\rm TFL}$), identified at the transition between the ohmic and trap-filled region, determines the trap density ($N_{\rm trap}$), and it can be calculated by the following equation [3]:

$$N_{\text{trap}} = \frac{2\epsilon\epsilon_0 V_{\text{TFL}}}{eL^2} \tag{1}$$

where ε is the relative dielectric constant of CsPbBr₃ (22),^[49] ε_0 is the vacuum dielectric constant (8.85 × 10⁻¹² F m⁻¹), e is the elementary charge, and L is the thickness of the wafer (1 mm). The $N_{\rm trap}$ of the target CsPbBr₃ wafer has been reduced to 2.82 × 10¹⁰ cm⁻³, which is lower than that of the control CsPbBr₃ wafer (5.46 × 10¹⁰ cm⁻³). To investigate the interaction between CsPbBr₃ and 2-bromonaphthalene, X-ray photoelectron spectroscopy (XPS) has been performed. As shown in Figure 2h, a downshift in the binding energies of the Pb 4f core levels indicates an increased electron cloud density within the lattice, which may be

Table 1. Resistivity and $\mu\tau$ products of CsPbBr₃ wafers.

Sample	Molar Ratio of 2-bromonaphthalene				
	0%	1%	3%	5%	10%
resistivity (Ω cm)	1.23 × 10 ⁹	2.36 × 10 ⁹	4.89 × 10 ⁹	5.21 × 10 ⁹	7.65×10^9
$\mu \tau$ product (cm ² V ⁻¹)	7.95×10^{-4}	2.38×10^{-3}	3.97×10^{-3}	2.60×10^{-3}	1.95×10^{-3}

16163028, 2025, 33. Downloaded from https://advanced.onlinelibrary.wiley.com/doi/10.1002/adfm.202500039 by Fudan University, Wiley Online Library on [28.09/2025]. See the Terms and Conditions (https://onlinelibrary.wiley

conditions) on Wiley Online Library for rules of use; OA articles are governed by the applicable Creative Commons Licens

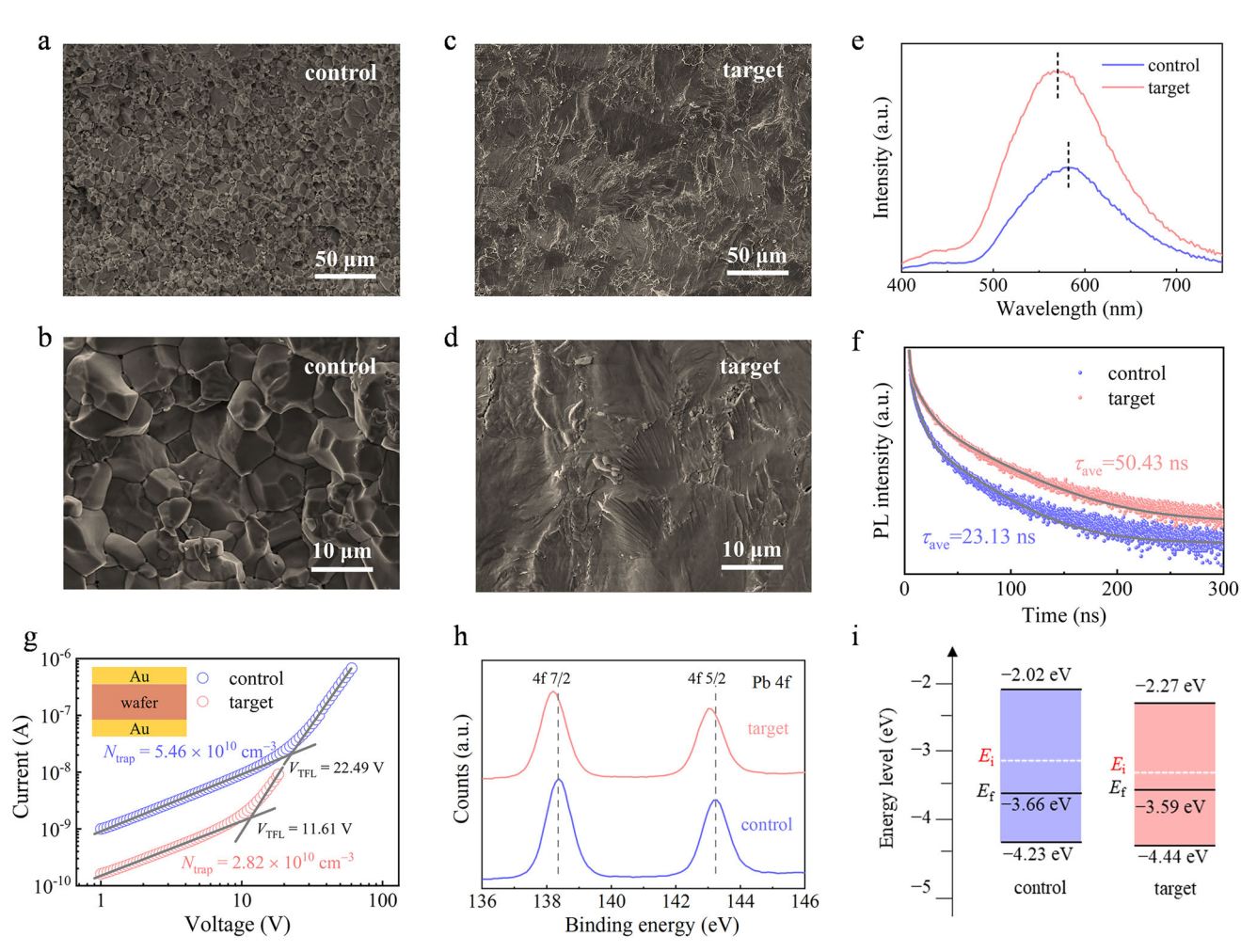


Figure 2. Cross-sectional morphology images of a,b) control and c,d) target CsPbBr₃ wafers. e) Photoluminescence spectra of control and target CsPbBr₃ wafers. f) Time-resolved photoluminescence spectra of the control and target CsPbBr3 wafers. g) Space-charged-limited current curves of the control and target CsPbBr₃ wafers. h) X-ray photoelectron spectroscopy Pb 4f spectra of the control and target CsPbBr₃ wafers. i) Schematic energy band diagrams of the control and target CsPbBr3 wafers.

attributed to the formation of coordination bonds between uncoordinated Pb2+ and 2-bromonaphthalene molecules, thus affirming the successful anchoring of 2-bromonaphthalene. To investigate the energy levels of the control and target CsPbBr3 wafers, UV photoelectron spectroscopy (UPS) measurements have been carried out (Figures S8, Supporting Information). The valence band maxima of the control and target CsPbBr₂ wafers are located at -4.23 and -4.44 eV, respectively. The work functions of the control and target CsPbBr3 wafers are 3.66 and 3.59 eV, respectively. The energy level diagram, shown in Figure 2i, has been constructed based on the UPS spectra and absorbance spectra (Figure S9, Supporting Information). The Fermi level of the control CsPbBr₃ wafer is -3.66 eV, which is 0.54 eV below the mid-gap position (E_i). In contrast, the Fermi level of the target CsPbBr₃ wafer is -3.59 eV, only 0.24 eV below the corresponding E_i , indicating either intrinsic or weak p-type electronic properties for the target CsPbBr3 wafer. This shift is likely due to the incorporation of 2-bromonaphthalene, which reduces interfacial defects and results in a more balanced electronic structure. Intrinsic semiconductors typically exhibit low free charge carrier

concentration, resulting in low dark current and reduced detector noise.[31,50]

As illustrated in Figure 3a, the coordination ability of 2bromonaphthalene enables it to anchor to the surface and grain boundaries of the CsPbBr3 wafer through coordination bonds, facilitated by electron transfer from the electron-rich bromine atoms to uncoordinated Pb2+, which is the primary deep-level defects at the surface and grain boundaries of the perovskite.^[51] The defects (V_{Br}⁺) located at the grain boundaries provide migration pathways for Br⁻ ions (Figure 3b), leading to enhanced ionic conductivity, increased dark current, and substantial current baseline drift, all of which deteriorate device performance and compromise long-term operational stability. In contrast, the interaction between 2-bromonaphthalene and under-coordinated Pb^{2+} reduces the concentration of V_{Br}^{+} (Figure 3c), thereby decreasing the available ion migration pathways. The I-V sweep loops of the Au/CsPbBr₃/Au devices, based on both the control and target CsPbBr3 wafers, are measured within a bias range of -50-50 V, as shown in Figure 3d. The device based on the control CsPbBr3 wafer exhibits I-V hysteresis across the entire

16163028, 2025, 33, Downloaded from https://advanced.onlinelibrary.wiley.com/doi/10.1002/adfm.202500039 by Fudan University, Wiley Online Library on [28.09/2025]. See the Terms and Conditions (https://online.com/doi/10.1002/adfm.202500039).

conditions) on Wiley Online Library for rules of use; OA articles are governed by the applicable Creative Commons

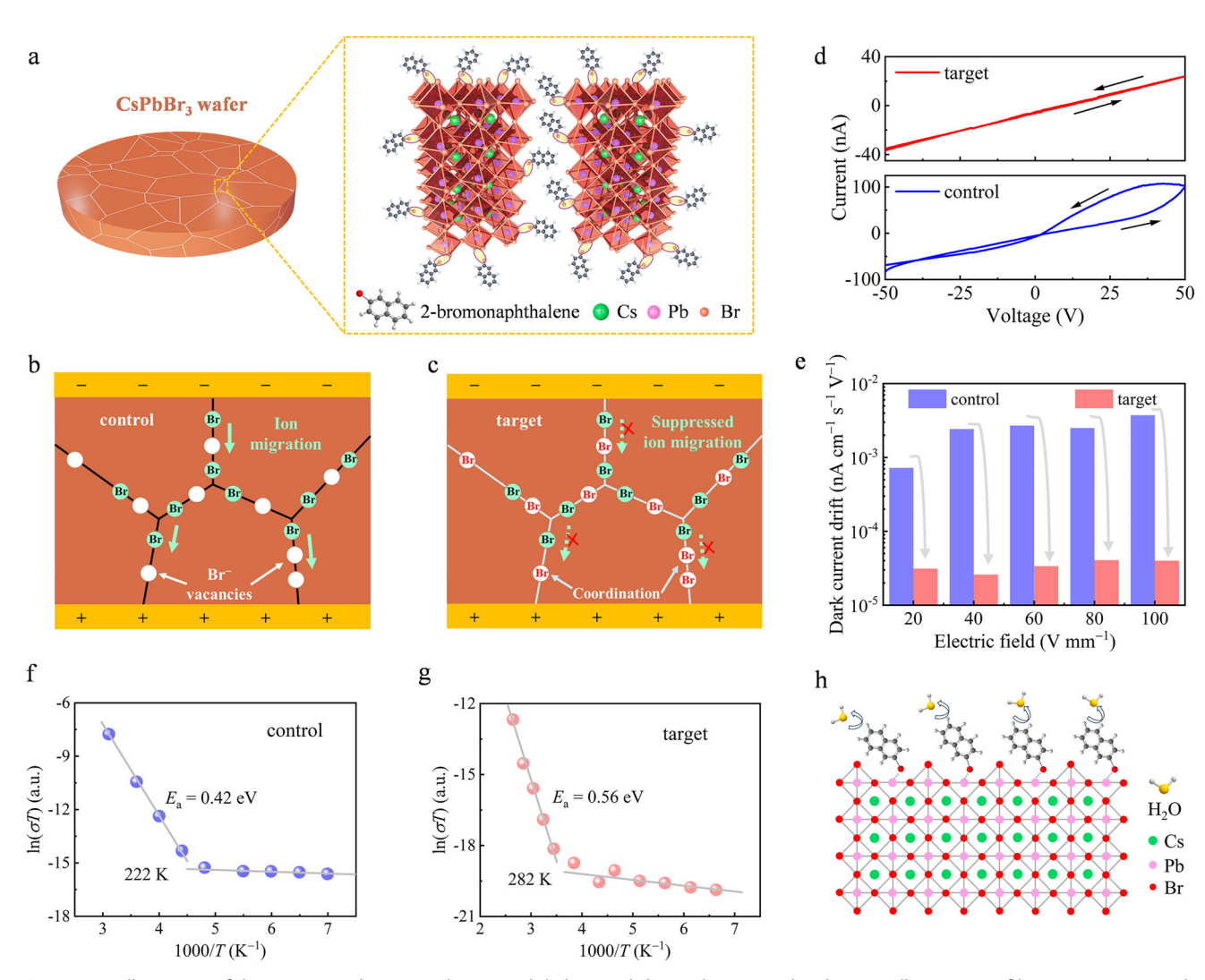


Figure 3. a) Illustration of the interaction between 2-bromonaphthalene and the CsPbBr₃ crystal. Schematic illustrations of b) ion migration in the control CsPbBr₃ wafer and c) suppressed ion migration in the target CsPbBr₃ wafer. d) *I–V* sweep loops of the control and target CsPbBr₃ wafer-based devices. e) Comparison of dark current drifts for devices based on the control and target CsPbBr₃ wafers under various electric fields ranging from 20 to 100 V mm⁻¹. Ion activation energies for the f) control and g) target CsPbBr₃ wafers. h) Schematic of the moisture resistance mechanism.

voltage range, whereas the device based on the target CsPbBr₃ wafer shows negligible hysteresis. Additionally, the stability of the dark current under various electric fields, ranging from 20 to 100 V mm⁻¹, has been characterized (Figure S10, Supporting Information). The dark current of the target device remains more stable compared to that of the control device. The dark current drift (*D*) of the device can be calculated using the following equation:^[35]

$$D = \frac{I_{\text{finish}} - I_{\text{begin}}}{tAE} \tag{2}$$

where $I_{\rm finish}$ and $I_{\rm begin}$ are the currents at the end and beginning of the measurement period, respectively, E is the applied electric field, A is the device area, and t is the test duration. The dark current drift of the control CsPbBr₃ wafer is 3.73×10^{-3} nA cm⁻¹ s⁻¹ V⁻¹ at 100 V mm⁻¹. In contrast, for the target

CsPbBr $_3$ wafer under the same condition, the dark current drift is significantly reduced by two orders of magnitude, as shown in Figure 3e. The negligible hysteresis in the I-V sweep loop and the low dark current drift both indicate the suppression of ion migration in the target CsPbBr $_3$ wafer. Furthermore, ion migration in the wafers has been quantitatively evaluated by determining the ion activation energy (E_a), calculated using the Nernst–Einstein equation: [52]

$$\sigma\left(T\right) = \frac{\sigma_0}{T} \exp\left(-\frac{E_a}{kT}\right) \tag{3}$$

where k is the Boltzmann constant, σ_0 is a constant, and T is the temperature. Generally, at low temperatures, electronic conduction is the primary cause of conductivity as the ion migration is suppressed. For the control CsPbBr₃ wafer, the ion conductivity begins to dominate above 222 K, with an E_a of

16163028, 2025, 33, Downloaded from https://advanced.onlinelibrary.wiley.com/doi/10.1002/adfm.202500039 by Fudan University, Wiley Online Library on [28.09/2025]. See the Terms and Conditions (https://onlin

conditions) on Wiley Online Library for rules of use; OA articles are governed by the applicable Creative Commons License

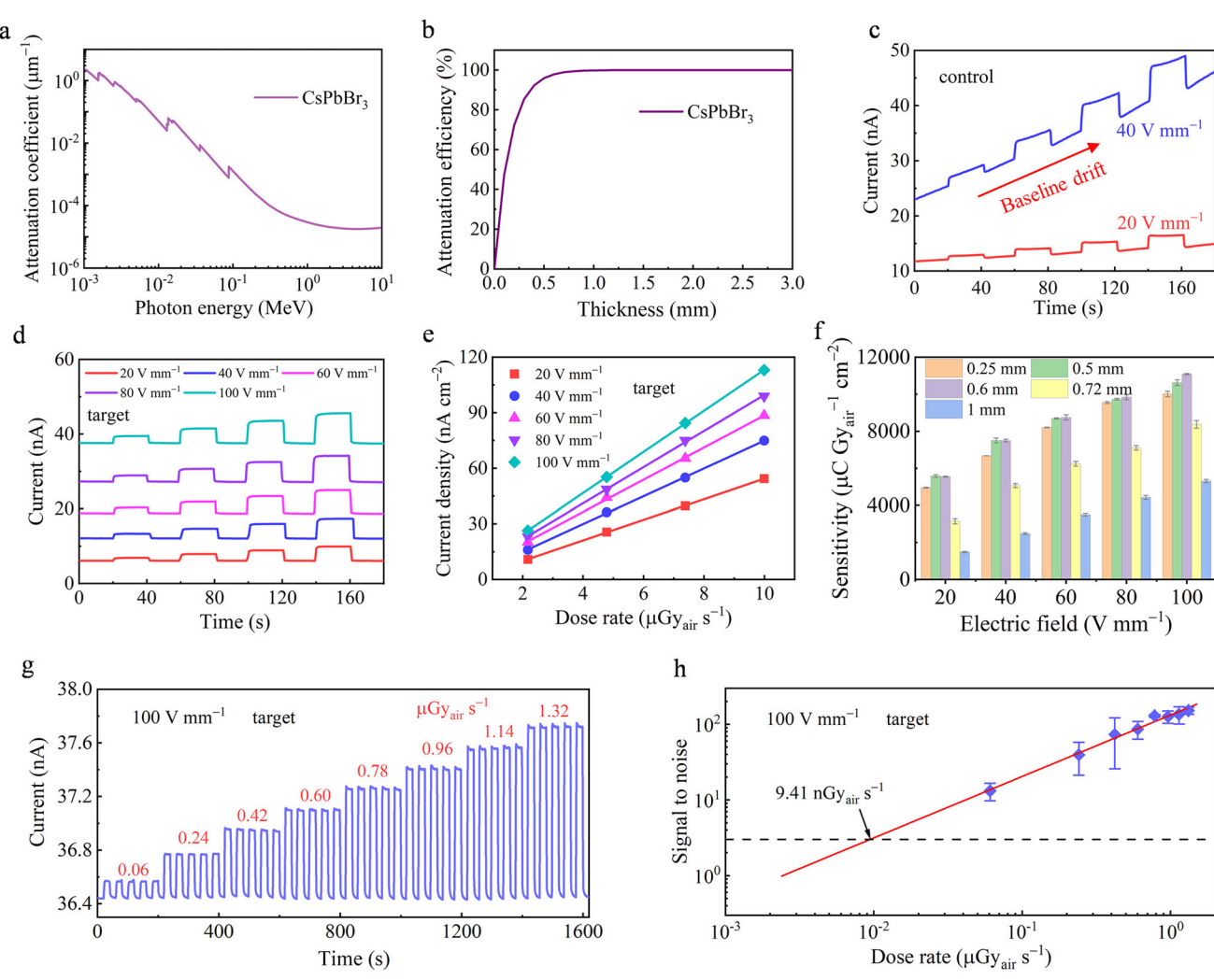


Figure 4. a) Attenuation coefficients of CsPbBr₃ as a function of X-ray photon energy. b) Attenuation efficiency of CsPbBr₃ for 40 keV X-ray photons versus thickness. c) Time-dependent X-ray responses of the detector based on the control CsPbBr₃ wafer with a thickness of 1 mm under electric fields of 20 and 40 V mm⁻¹. d) Time-dependent X-ray responses and e) current density as a function of X-ray dose rates for the X-ray detector based on the target CsPbBr₃ wafer with a thickness of 0.6 mm. f) Sensitivity statistic for the X-ray detectors based on target CsPbBr₃ wafers with different thicknesses. g) X-ray response curve under different X-ray dose rates and h) dose rate-dependent single-to-noise (SNR) ranging from 0.06 to 1.32 μGy_{air} s⁻¹ at 100 V mm⁻¹ for the X-ray detector based on the target CsPbBr₃ wafer with a thickness of 0.6 mm.

0.42 eV (Figure 3f). In contrast, the conductivity of the device based on the target CsPbBr3 wafer reveals a conductivity transition at 282 K, with a higher E_a of 0.56 eV (Figure 3g), confirming the suppressed ion migration upon the incorporation of 2-bromonaphthalene. The abovementioned results demonstrate that the reduced interfacial defects, resulting from the interaction between 2-bromonaphthalene and uncoordinated Pb2+ (halide vacancy), effectively inhibit ionic migration in the target CsPbBr₃ wafer. Moreover, the introduction of 2-bromonaphthalene also enhances the moisture resistance of the target CsPbBr₃ wafer. As shown in Figure S11 (Supporting Information), the control CsPbBr3 wafer exhibits a relatively small contact angle of 50°, whereas the target CsPbBr3 wafer presents a larger contact angle of 98°. A possible mechanism for the enhanced moisture resistance is illustrated in Figure 3h. The coordination ability of 2-bromonaphthalene enables it to anchor onto the surface of the CsPbBr₃ wafer, thereby reducing the number of moisture absorption sites. Consequently, the interaction between ambient water molecules and the perovskite wafer is effectively inhibited. This improved moisture resistance is crucial for maintaining wafer stability under ambient conditions, thereby supporting its performance and longevity in X-ray detection applications.

Devices with an Au/CsPbBr₃/Au symmetric electrode structure have been fabricated to evaluate the X-ray detection performance (Figure S4, Supporting Information). The attenuation coefficient of CsPbBr₃, obtained from the NIST database, is shown in **Figure 4a**.^[39] Figure 4b illustrates the attenuation efficiency of CsPbBr₃ at different thicknesses for 40 keV X-ray photons. Figure 4c displays the time-dependent X-ray responses of the detector based on the control CsPbBr₃ wafer with a thickness of 1 mm under electric fields of 20 and 40 V mm⁻¹. The detector exhibits significant baseline drift over time due to ion migration,

with the dark current increasing from 11.76 to 14.95 nA at 20 V mm⁻¹ and from 23.02 to 46.47 nA at 40 V mm⁻¹. This persistent signal drift compromises the stability of the detector and reduces its accuracy in measuring X-ray intensity. In contrast, as shown in Figure 4d and Figure S13 (Supporting Information), the detectors based on the target CsPbBr3 wafer (with thickness ranging from 0.25 to 1 mm) maintain stable dark current baselines across a wide range of electric fields from 20 to 100 V mm⁻¹. This stability further demonstrates the effective suppression of ionic migration within the CsPbBr3 wafers, thereby reducing the ionic conductivity and stabilizing the dark current baseline. Additionally, the photocurrent response of the target CsPbBr3 wafer devices gradually increases with rising external electric field (from 20 to 100 V mm⁻¹) and X-ray dose rates (from 2.17 to 9.99 μ Gy_{air} s⁻¹). The variations in net photocurrent density with dose rate under electric fields from 20 to 100 V mm⁻¹ are shown in Figure 4e and Figure S14 (Supporting Information), all of which exhibit a linear relationship with the X-ray dose rates.

The sensitivity of the X-ray detector under different electric fields can be determined from the slope of the linear fitting according to the equation:[32]

$$S = \frac{I_{\rm R}}{DA} \tag{4}$$

where S is the sensitivity, I_{R} is the signal current, D is the X-ray dose rate, and A is the active area of the device. Figure 4f illustrates the sensitivity statistic for the devices based on the target CsPbBr3 wafers with different thicknesses. As the wafer thickness increases from 0.25 to 1 mm, the device sensitivity initially increases and then decreases, reflecting the combined effects of wafer thickness, X-ray attenuation efficiency, and electric field on device performance. In thinner wafers, limited X-ray attenuation efficiency reduces sensitivity. Conversely, in thicker wafers, increased thickness under a constant electric field decreases carrier collection efficiency, thereby lowering sensitivity. The statistic demonstrates that devices with thicknesses of 0.5 and 0.6 mm exhibit higher sensitivity than others. When the electric field is low, the 0.6 mm device, despite its higher X-ray attenuation efficiency relative to the 0.5 mm device, exhibits slightly reduced sensitivity due to limited carrier transport distance. However, as the electric field intensity increases, the sensitivity of the 0.6 mm device surpasses that of the 0.5 mm device when the electric field reaches 60 V mm⁻¹, leveraging the advantage of the higher X-ray attenuation efficiency. Based on the comprehensive analysis, the X-ray detector based on the target CsPbBr₃ wafer with a thickness of 0.6 mm achieves an optimal balance, ensuring adequate absorption of 40 keV X-ray photons while maintaining efficient carrier collection. The sensitivity of the device based on the target CsPbBr3 wafer with a thickness of 0.6 mm is measured to be 11090 μ C Gy_{air}⁻¹ cm⁻² under an electric field of 100 V mm⁻¹. This high sensitivity is even comparable to that of previously reported CsPbBr₃ SC counterparts (Table S1, Supporting Information), indicating the excellent photoelectric performance of the target CsPbBr₃ polycrystalline wafer device.

The detection limit is a crucial parameter for X-ray detectors, representing the minimum X-ray dose rate that can be reliably distinguished from background noise. As shown in Figure S15 (Supporting Information), a practical procedure of the calculated method (I_{dark} & S method) for the detection limit is provided.^[53] Under an electric field of 100 V mm⁻¹, the sensitivity of the target CsPbBr₃ wafer (0.6 mm) X-ray detector has been measured to be $11090\,\mu\text{C Gy}_{air}^{-1}\,\text{cm}^{-2}$. The standard deviation of the dark current $(\sigma_{L_{lock}})$, is ≈ 1.68 pA, calculated using the dark current after a long time of biasing (Figure S15c, Supporting Information), which yields the detection limit of net current (I_{limit}) to be 5.53 pA. Consequently, the detection limit is calculated to be 7.05 nGy_{air} s^{-1} under an electric field of 100 V mm⁻¹. Additionally, the commonly used method based on the linear extrapolation of the dose-ratedependent SNR was also employed for comparison.[35] The SNR is calculated using the following formula:[35]

$$SNR = \frac{I_{\text{signal}}}{I_{\text{poiso}}} \tag{5}$$

where $I_{\rm signal}$ is the difference between the average photocurrent and the average dark current and $I_{\rm noise}$ presents the standard deviation of the photocurrent. Figure 4g illustrates the response of the CsPbBr₃ wafer X-ray detector (thickness: 0.6 mm) under on/off X-ray radiation at various dose rates (0.06–1.32 μ Gy_{air} s⁻¹), under an applied electric field of 100 V mm⁻¹. Figure 4h shows the corresponding dose rate-dependent SNR, from which the detection limit is determined to be as low as 9.41 nGy_{air} s⁻¹, highlighting the potential of the target CsPbBr3 wafer for high-performance Xray detection. Notably, the detection limits calculated using both the traditional SNR-based approach and the $I_{\rm dark}$ & S method are very similar. This consistency suggests that, although the underlying principles differ, the practical outcomes of the two methods align closely in our specific case. Importantly, the I_{dark} & S method provides a more rigorous statistical basis consistent with the International Union of Pure and Applied Chemistry (IUPAC) definition, as it accounts for the standard deviation of the background signal without relying on the time variable inherent in the dose rate.[53]

Maintaining a stable output detection signal over prolonged periods is a crucial performance metric for X-ray detectors in practical applications. The target CsPbBr3 wafer X-ray detector maintains a stable current signal, with no baseline drift or photocurrent attenuation observed (Figure 5a,b). The outstanding operational and irradiation stability further confirm the effective suppression of ion migration within the target CsPbBr₂ wafer and underscore the potential of the target CsPbBr3 wafer Xray detectors for high-quality X-ray imaging. To assess the X-ray imaging capabilities of the CsPbBr3 wafer X-ray detectors, the devices are employed in scanning imaging experiments. Figure 5c schematically illustrates the X-ray imaging process for a plastic box containing a steel nut (Figure \$16, Supporting Information). In this setup, the object is positioned between the X-ray source and the detector and is maneuvered using an x-y scanning stage. By collecting the response current generated by transmitted Xray photons at various (x, y) coordinates, an X-ray image can be obtained. To compare the performance of the control and target CsPbBr3 wafer X-ray detectors, X-ray images of a plastic box containing a concealed steel nut are taken under electric fields of 10 and 50 V mm⁻¹ at an X-ray dose rate of 4.30 μ Gy_{air} s⁻¹. Under a lower electric field of 10 V mm⁻¹, the control CsPbBr₃ wafer X-ray detector shows an indistinct X-ray image with a low SNR (Figure 5d). In contrast, the target CsPbBr₃ wafer X-ray

16163028, 2025, 33. Downloaded from https://advanced.onlinelibrary.wiley.com/doi/10.1002/adfm.202500039 by Fudan University, Wiley Online Library on [28.09/2025]. See the Terms and Conditions (https://online.com/doi/10.1002/adfm.202500039 by Fudan University, Wiley Online Library on [28.09/2025]. See the Terms and Conditions (https://online.com/doi/10.1002/adfm.202500039 by Fudan University, Wiley Online Library on [28.09/2025]. See the Terms and Conditions (https://online.com/doi/10.1002/adfm.202500039 by Fudan University, Wiley Online Library on [28.09/2025]. See the Terms and Conditions (https://online.com/doi/10.1002/adfm.202500039 by Fudan University, Wiley Online Library on [28.09/2025]. See the Terms and Conditions (https://online.com/doi/10.1002/adfm.202500039 by Fudan University, Wiley Online Library on [28.09/2025]. See the Terms and Conditions (https://online.com/doi/10.1002/adfm.202500039 by Fudan University, Wiley Online Library on [28.09/2025]. See the Terms and Conditions (https://online.com/doi/10.1002/adfm.202500039 by Fudan University, Wiley Online Library on [28.09/2025]. See the Terms and Conditions (https://online.com/doi/10.1002/adfm.202500039 by Fudan University, Wiley Online Library on [28.09/2025]. See the Terms and Conditions (https://online.com/doi/10.1002/adfm.202500039 by Fudan University).

conditions) on Wiley Online Library for rules of use; OA articles are governed by the applicable Creative Commons License

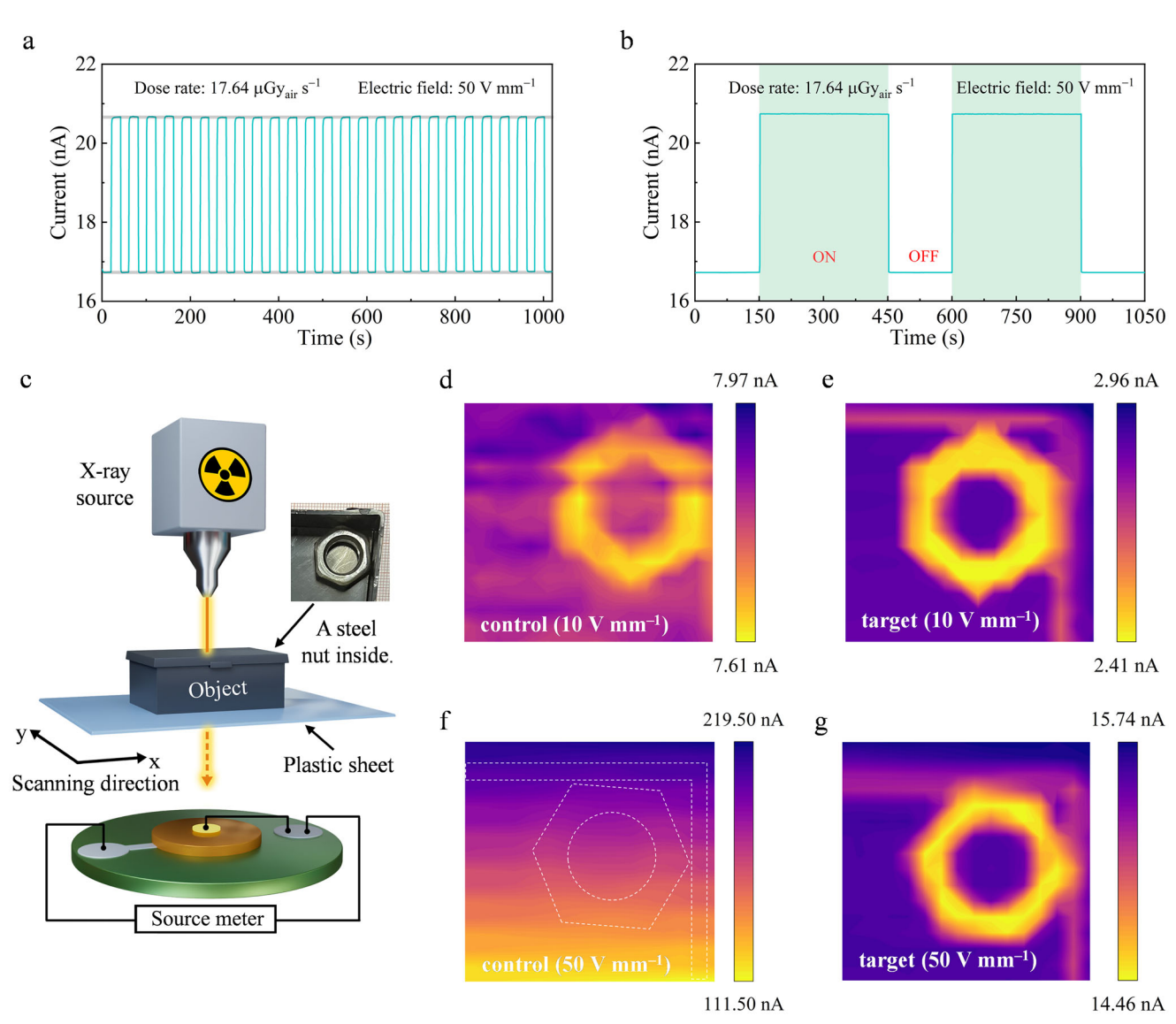


Figure 5. a) Time-dependent photocurrent response stability and b) long-term operational stability under continuous X-ray irradiation of the target CsPbBr₃ wafer-based X-ray detector (thickness: 1 mm) at a dose rate of 17.64 µGy_{air} s⁻¹ and an electric field of 500 V cm⁻¹. c) Schematic illustration of the X-ray imaging system employing the CsPbBr₃ wafer-based X-ray detector. d-g) X-ray images of a closed plastic box containing a steel nut.

detector generates a clear, high-SNR X-ray image (Figure 5e), demonstrating superior sensitivity and stability. Notably, the edge of the box is also clearly discernible, providing a distinct contrast with the imaging of the nut. This demonstrates that the target X-ray detector can sensitively differentiate between strong and weak X-ray signals, highlighting its high sensitivity. To further evaluate the imaging capability under high electric field intensity, the applied electric field is increased to 50 V mm⁻¹. As shown in Figure 5f, the control X-ray detector fails to produce a discernible image, with the X-ray signal completely submerged. This failure is attributed to ion migration within the control device at high electric fields, which results in an elevated dark current that overwhelms the X-ray response signal. Conversely, the target X-ray detector exhibits a clear image with well-defined contours of the object under 50 V mm⁻¹ (Figure 5g), further validating the excellent sensitivity, stability, and operational robustness of the target CsPbBr3 wafer X-ray detector under high electric field.

3. Conclusion

In summary, CsPbBr3 wafers with suppressed ion migration have been successfully prepared using a hot-pressing method. The incorporation of 2-bromonaphthalene enables effective passivation of interface defects, thereby suppressing ion migration and enhancing charge transport properties. As a result, the target CsPbBr₃ wafer exhibits a high resistivity of $4.89 \times 10^9 \Omega$ cm, an ion migration activation energy of 0.56 eV, negligible dark current drift of 4.01×10^{-5} nA cm⁻¹ s⁻¹ V⁻¹ under 100 V mm⁻¹, and exceptional charge carrier transport with a high $\mu\tau$ product of $3.97 \times 10^{-3} \text{ cm}^2 \text{ V}^{-1}$. The resulting Au/CsPbBr₃/Au X-ray detector achieves a high sensitivity of 11090 μC Gy_{air}⁻¹ cm⁻², a

16163028, 2025, 33, Downloaded from https://advanced.onlinelibrary.wiley.com/doi/10.1002/adfm.202500039 by Fudan University, Wiley Online Library on [28.09/2025]. See the Terms and Conditions (https://onlinelibrary.wiley

conditions) on Wiley Online Library for rules of use; OA articles are governed by the applicable Creative Commons

low detection limit of 9.41 nGy_{air} s⁻¹ under an electric field of 100 V mm⁻¹, along with long-term operational stability and highcontrast X-ray imaging capabilities. This work presents an effective interface passivation strategy for the scalable fabrication of perovskite wafers with suppressed ion migration and stable X-ray detection, highlighting their potential for advanced X-ray imaging applications.

4. Experimental Section

Details of the experiments and methods are provided in the Supporting Information.

Supporting Information

Supporting Information is available from the Wiley Online Library or from the author.

Acknowledgements

This work was financially supported by the National Natural Science Foundation of China (Grant Nos. 62075223, 62211540009, 52425308, 62374035, 12211530438, and 92263106), the State Key Laboratory of Particle Detection and Electronics (Grant No. SKLPDE-KF-202410), State Key Laboratory of Quantum Optics and Quantum Optics Devices (Grant No. KF202304).

Conflict of Interest

The authors declare no conflict of interest.

Data Availability Statement

The data that support the findings of this study are available in the supplementary material of this article.

Keywords

CsPbBr₃ wafer, defect passivation, hot-pressing, ion migration, X-ray detection

> Received: January 1, 2025 Revised: February 10, 2025 Published online: March 17, 2025

- [1] H. Wei, Y. Fang, P. Mulligan, W. Chuirazzi, H.-H. Fang, C. Wang, B. R. Ecker, Y. Gao, M. A. Loi, L. Cao, J. Huang, Nat. Photonics 2016, 10,
- [2] H. Li, Y. Lei, G. Peng, Q. Wang, Z. Li, H. Wang, G. Wang, Z. Jin, Adv. Funct. Mater. 2022, 32, 2208199.
- [3] W.-G. Li, X.-D. Wang, Y.-H. Huang, D.-B. Kuang, Adv. Mater. 2023, 35,
- [4] X. Yang, Y.-H. Huang, X.-D. Wang, W.-G. Li, D.-B. Kuang, Angew. Chem., Int. Ed. 2022, 61, 202204663.
- [5] Y. He, I. Hadar, M. G. Kanatzidis, Nat. Photonics 2022, 16, 14.
- [6] Z. Li, F. Zhou, H. Yao, Z. Ci, Z. Yang, Z. Jin, Mater. Today 2021, 48,
- [7] X. Zhang, D. Chu, B. Jia, Z. Zhao, J. Pi, Z. Yang, Y. Li, J. Hao, R. Shi, X. Dong, Y. Liang, J. Feng, A. Najar, Y. Liu, S. Liu, Adv. Mater. 2024, 36, 2305513.

- [8] Y. Zhang, J. Hao, Z. Zhao, J. Pi, R. Shi, X. Li, N. Yuan, J. Ding, S. Liu, Y. Liu, Adv. Mater. **2024**, 36, 2310831.
- [9] H. Wei, J. Huang, Nat. Commun. 2019, 10, 1066.
- [10] M. Li, H. Li, W. Li, B. Li, T. Lu, X. Feng, C. Guo, H. Zhang, H. Wei, B. Yang, Adv. Mater. 2022, 34, 2108020.
- [11] B. Yang, W. Pan, H. Wu, G. Niu, J.-H. Yuan, K.-H. Xue, L. Yin, X. Du, X.-S. Miao, X. Yang, Q. Xie, J. Tang, Nat. Commun. 2019, 10,
- [12] W. Qian, X. Xu, J. Wang, Y. Xu, J. Chen, Y. Ge, J. Chen, S. Xiao, S. Yang, Matter 2021, 4, 942.
- [13] P. Ran, L. Yang, T. Jiang, X. Xu, J. Hui, Y. Su, C. Kuang, X. Liu, Y. Yang, Adv. Mater. 2022, 34, 2205458.
- [14] X. He, M. Xia, H. Wu, X. Du, Z. Song, S. Zhao, X. Chen, G. Niu, J. Tang, Adv. Funct. Mater. 2022, 32, 2109458.
- [15] D. Xin, S. Dong, M. Zhang, S. Tie, J. Ren, L. Lei, P. Yu, J. Zhu, Y. Zhao, X. Zheng, J. Phys. Chem. Lett. 2022, 13, 371.
- [16] A. Ciavatti, R. Sorrentino, L. Basiricò, B. Passarella, M. Caironi, A. Petrozza, B. Fraboni, Adv. Funct. Mater. 2021, 31, 2009072.
- [17] B. Dou, J. B. Whitaker, K. Bruening, D. T. Moore, L. M. Wheeler, J. Ryter, N. J. Breslin, J. J. Berry, S. M. Garner, F. S. Barnes, S. E. Shaheen, C. J. Tassone, K. Zhu, M. F. A. M. van Hest, ACS Energy Lett. 2018, 3,
- [18] Y. Chai, Z. Juan, Y. Wu, Y. Liu, X. Li, ACS Appl. Electron. Mater. 2023, 5, 544.
- [19] Y. Haruta, T. Ikenoue, M. Miyake, T. Hirato, Appl. Phys. Express 2019, 12 085505
- [20] M. Hu, S. Jia, Y. Liu, J. Cui, Y. Zhang, H. Su, S. Cao, L. Mo, D. Chu, G. Zhao, K. Zhao, Z. Yang, S. Liu, ACS Appl. Mater. Interfaces 2020, 12,
- [21] X. Zhao, S. Wang, F. Zhuge, Y. Song, T. Aoki, W. Dong, M. Fu, G. Meng, Z. Deng, R. Tao, X. Fang, J. Phys. Chem. Lett. 2022, 13, 3008.
- [22] J. Yu, Y. Luo, N. Tian, Y. Liu, Z. Yang, J. Pi, L. Li, R. Zeng, C. Wang, S. Liu, Adv. Mater. 2025, 37, 2413709.
- [23] M. Zhang, L. Lei, W. Zhao, D. Yang, X. Zheng, W.-H. Zhang, J. Phys. Chem. C 2023, 127, 16219.
- [24] Y. Liu, Z. Xu, Z. Yang, Y. Zhang, J. Cui, Y. He, H. Ye, K. Zhao, H. Sun, R. Lu, M. Liu, M. G. Kanatzidis, S. Liu, Matter 2020, 3, 180.
- [25] S. Tie, W. Zhao, D. Xin, M. Zhang, J. Long, Q. Chen, X. Zheng, J. Zhu, W.-H. Zhang, Adv. Mater. 2020, 32, 2001981.
- [26] Y. Zhang, Y. Liu, Z. Xu, H. Ye, Z. Yang, J. You, M. Liu, Y. He, M. G. Kanatzidis, S. Liu, Nat. Commun. 2020, 11, 2304.
- [27] M. I. Saidaminov, O. F. Mohammed, O. M. Bakr, ACS Energy Lett. 2017. 2. 889.
- [28] X. Zhang, X. Ren, B. Liu, R. Munir, X. Zhu, D. Yang, J. Li, Y. Liu, D.-M. Smilgies, R. Li, Z. Yang, T. Niu, X. Wang, A. Amassian, K. Zhao, S. Liu, Energy Environ. Sci. 2017, 10, 2095.
- [29] R. Zhuang, X. Wang, W. Ma, Y. Wu, X. Chen, L. Tang, H. Zhu, J. Liu, L. Wu, W. Zhou, X. Liu, Y. Yang, Nat. Photonics 2019, 13, 602.
- [30] Y. Xiao, C. Xue, X. Wang, Y. Liu, Z. Yang, S. Liu, ACS Appl. Mater. Interfaces 2022, 14, 54867.
- [31] H. Li, J. Song, W. Pan, D. Xu, W. Zhu, H. Wei, Bai Yang, Adv. Mater. **2020**, 32, 2003790.
- [32] L. Clinckemalie, D. Valli, M. B. J. Roeffaers, J. Hofkens, B. Pradhan, E. Debroye, ACS Energy Lett. 2021, 6, 1290.
- [33] R. Shi, J. Pi, D. Chu, B. Jia, Z. Zhao, J. Hao, X. Zhang, X. Dong, Y. Liang, Y. Zhang, Y. Liu, S. Liu, ACS Energy Lett. 2023, 8,
- [34] P. Zhang, Y. Hua, Y. Xu, Q. Sun, X. Li, F. Cui, L. Liu, Y. Bi, G. Zhang, X. Tao, Adv. Mater. 2022, 34, 2106562.
- [35] F. Cui, P. Zhang, L. Zhang, Y. Hua, X. Sun, X. Li, G. Zhang, X. Tao, Chem. Mater. 2022, 34, 9601.
- [36] Z. Xu, H. Xi, X. Sun, H. Liu, J. Liu, Y. Ba, D. Chen, G. Zhang, C. Zhang, X. Ma, Y. Hao, Adv. Funct. Mater. 2024, 34, 2400817.
- [37] E. Hong, Z. Li, X. Zhang, X. S. Fang, Adv. Funct. Mater. 2025, 35, 2412189.

© 2025 Wiley-VCH GmbH



www.advancedsciencenews.com



www.afm-journal.de

16163028, 2025, 33, Downloaded from https://advanced.onlinelibrary.wiley.com/doi/10.1002/adfm.202500039 by Fudan University, Wiley Online Library on [28.09/2025]. See the Terms

conditions) on Wiley Online Library for rules

of use; OA

articles are governed by the applicable Creative Commons

- [38] Y. Hua, G. Zhang, X. Sun, P. Zhang, Y. Hao, Y. Xu, Y. Yang, Q. Lin, X. Li, Z. Zhai, F. Cui, H. Liu, J. Liu, X. Tao, *Nat. Photonics* 2024, 18, 870.
- [39] X. Du, Y. Liu, W. Pan, J. Pang, J. Zhu, S. Zhao, C. Chen, Y. Yu, Z. Xiao, G. Niu, J. Tang, Adv. Mater. 2022, 34, 2110252.
- [40] Q. Guo, J. Duan, J. Zhang, Q. Zhang, Y. Duan, X. Yang, B. He, Y. Zhao, Q. Tang, Adv. Mater. 2022, 34, 2202301.
- [41] Z. Qu, Y. Zhao, F. Ma, L. Mei, X.-K. Chen, H. Zhou, X. Chu, Y. Yang, Q. Jiang, X. Zhang, J. You, Nat. Commun. 2024, 15, 8620.
- [42] X. Zhao, S. Wang, Y. Song, T. Aoki, V. Gnatyuk, L. You, Z. Deng, R. Tao, X. Fang, G. Meng, Appl. Phys. Lett. 2024, 125, 083507.
- [43] X. Zhang, Z. Li, E. Hong, T. Yan, X. S. Fang, Adv. Mater. 2025, 37, 2412014.
- [44] G. Tong, T. Chen, H. Li, L. Qiu, Z. Liu, Y. Dang, W. Song, L. K. Ono, Y. Jiang, Y. Qi, *Nano Energy* **2019**, *65*, 104015.
- [45] M. Deng, Z. Li, S. Liu, X. S. Fang, L. Wu, Nat. Commun. 2024, 15, 8789.

- [46] L. Zheng, A. Nozariasbmarz, Y. Hou, J. Yoon, W. Li, Y. Zhang, H. Wu, D. Yang, T. Ye, M. Sanghadasa, K. Wang, B. Poudel, S. Priya, K. Wang, Nat. Commun. 2022, 13, 7399.
- [47] Y. Shao, Z. Xiao, C. Bi, Y. Yuan, J. Huang, Nat. Commun. 2014, 5, 5784.
- [48] L. Chen, H. Wang, W. Zhang, F. Li, Z. Wang, X. Wang, Y. Shao, J. Shao, ACS Appl. Mater. Interfaces 2022, 14, 10917.
- [49] M. I. Saidaminov, M. A. Haque, M. A. Haque, J. Almutlaq, S. Sarmah, X.-H. Miao, R. Begum, A. A. Zhumekenov, I. Dursun, N. Cho, B. Murali, O. F. Mohammed, T. Wu, O. M. Bakr, Adv. Opt. Mater. 2017, 5, 1600704.
- [50] H. Wei, D. DeSantis, W. Wei, Y. Deng, D. Guo, T. J. Savenije, L. Cao, J. Huang, Nat. Mater. 2017, 16, 826.
- [51] C. Luo, G. Zheng, X. Wang, F. Gao, C. Zhan, X. Gao, Q. Zhao, Energy Environ. Sci. 2023, 16, 178.
- [52] X. Feng, L. Zhang, B. Zhang, J. You, K. Li, H. Zeng, X. Wang, Z. Dai, S. Jia, H. Bao, S. Wang, S. Liu, Adv. Funct. Mater. 2024, 34, 2402166.
- [53] L. Pan, S. Shrestha, N. Taylor, W. Nie, L. R. Cao, *Nat. Commun.* 2021, 12, 5258.